ADVANCED MATERIALS INTERFACES
Open Access
www.advmatinterfaces.de

Extremely High Intrinsic Carrier Mobility and Quantum Hall Effect Of Single Crystalline Graphene Grown on Ge(110)

Wang Guo, Miao Zhang, Zhongying Xue, Paul K. Chu, Yongfeng Mei, Ziao Tian, and Zengfeng Di**

The successful synthesis of wafer-scale single crystalline graphene on semiconducting Ge substrate has been considered a significant breakthrough toward the manufacturing of graphene-based electronic and photonic devices; however, the assumed extremely high electrical mobility has not been found yet due to the lack of an adequate characterization method. Herein, state-of-the-art transfer methods are developed to encapsulate the single crystalline graphene, which is grown on semiconducting Ge(110), in two hexagonal boron nitride (hBN) flakes, then acquire its inherent electrical mobility precisely via edge-contact technique. It is found that single crystalline graphene grown on Ge(110) possesses a maximum carrier mobility of over 100 000 $cm^2 V^{-1} s^{-1}$ at low temperatures (2.3 K), which is superior to that obtained from graphene grown on other nonmetal substrates. Due to the extremely high mobility, well-defined quantum Hall effect and Shubnikov-de Haas oscillations can be observed at low temperatures as well. The study suggests that the excellent carrier mobility of graphene grown on Ge(110) may open an avenue to develop the practical graphene-based nanodevices with high performance.

1. Introduction

Graphene synthesized on semiconducting germanium (Ge) substrate by chemical vapor decomposition (CVD) enables the development of radio frequency transistors,[1–4] spintronic devices, and optical integrated devices with high performances.[5–7] Since the whole synthesis procedure avoids the use of metallic substrates,[8,9] it is compatible with modern semiconductor technology, thus permitting device downscaling and the extension of Moore's law.[10] In the past decade, single crystalline graphene has been successfully grown on Ge(110) and Ge(001),[11,12] and a number of technologies have been used to examine the charge transport properties of graphene, particularly their intrinsic carrier mobilities. For example, a mobility of only 1000 $cm^2 V^{-1} s^{-1}$ is determined for graphene grown on Ge substrate using the traditional polymer-assisted wet-transfer method.[1] The obtained value of carrier mobility is far below the expected one due to the inadequate transfer process. The carrier mobility increases to 7250 $cm^2 V^{-1} s^{-1}$ when gold-coated graphene film is directly exfoliated from the underlying Ge substrate by using thermal-release tape (TRT).[2] Recently, an indirect characterization, known as terahertz time domain spectroscopy (THz-TDS), has been performed to determine the carrier mobility across the graphene on the intrinsic Ge(110) wafer.[11] This noncontact and

W. Guo, M. Zhang, Z. Xue, Z. Tian, Z. Di
National Key Laboratory of Materials for Integrated Circuits
Shanghai Institute of Microsystem and Information Technology
Chinese Academy of Sciences
Shanghai 200050, China
E-mail: zatian@mail.sim.ac.cn; zfdi@mail.sim.ac.cn

W. Guo
Center of Materials Science and Optoelectronics Engineering
University of Chinese Academy of Sciences
Beijing 100049, China

P. K. Chu
Department of Physics
Department of Materials Science and Engineering
and Department of Biomedical Engineering
City University of Hong Kong
Tat Chee Avenue, Kowloon, Hong Kong 999077, China

Y. Mei
Department of Materials Science
Fudan University
Shanghai 200433, China

The ORCID identification number(s) for the author(s) of this article can be found under https://doi.org/10.1002/admi.202300482

DOI: 10.1002/admi.202300482

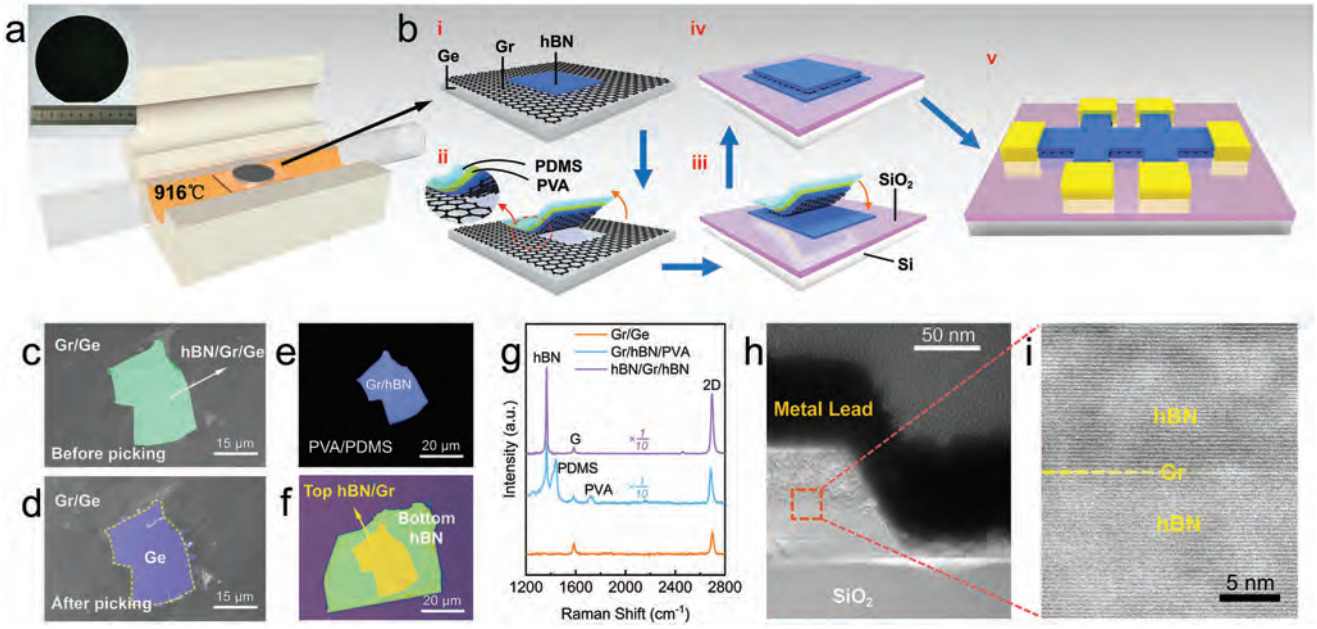

Figure 1. Formation of edge-contact Hall bar device based on hBN/graphene/hBN sandwich structure. a) The single crystalline graphene grown on Ge(110) substrate in a CVD furnace at 916 °C. b) Dry transfer process by van der Waals interactions: (i) hBN flake mechanically exfoliated on a slice of graphene/Ge(110) sample cutting from a wafer as shown in (a). (ii) Peel the graphene/hBN heterojunction directly with PVA/PDMS film; (iii) Transfer the heterojunction to another slice of hBN flake on SiO_2/Si substrate; (iv) Formation of hBN/graphene/hBN sandwich structure; (v) Fabrication of edge-contact Hall bar device. c) SEM image of an exfoliated hBN flake on graphene/Ge(110) (green area). d) SEM image of graphene/Ge(110) after the hBN/graphene is peeled from the substrate. The blue area illustrates the bare Ge substrate and the yellow dotted line shows the contour of the hBN flake. e) Optical image of the graphene/hBN transferred on PVA/PDMS. f) Optical image of hBN/graphene/hBN sandwich structure formed by releasing graphene/hBN on hBN covered SiO_2 substrate. g) Raman spectra showing the main formation steps of hBN/graphene/hBN sandwich structure including graphene/Ge (Gr/Ge), graphene/hBN/PVA (Gr/hBN/PVA), and hBN/graphene/hBN (hBN/Gr/hBN). h) Bright-field cross-section TEM image of the edge-contact geometry of the Hall bar device. i) Zoom in high-resolution cross-section STEM image from red box in h) showing the hBN/graphene/hBN sandwich structure.

nondestructive method shows the ultrahigh average mobility as 26351 $cm^2 V^{-1} s^{-1}$, even with the scattering effect of Ge substrate. However, a direct method to obtain the intrinsic carrier mobility of single crystalline graphene without the scattering effect of Ge substrate is still under demand.[13,14]

In this work, by using hBN flake, single crystalline graphene without any undesirable residues coming from the transfer process can be directly peeled from Ge(110) substrate due to the extremely weak adhesion between graphene and the Ge substrate.[15] After printing graphene onto another piece of mechanically exfoliated hBN flake, a sandwich heterojunction of hBN/graphene/hBN is formed, in which encapsulated graphene is protected from external moisture and air,[16] and the scattering effect from semiconducting Ge substrate can be excluded. The sandwich structure is able to eliminate the possibility of mobility deterioration caused by transfer and substrate-induced long-range scattering remarkably.[13,17,18] A Hall bar device fabricated with the edge-contact technique is demonstrated to have maximum electron (ϵ_e) and hole (ϵ_h) mobilities of 96 000 and 100 000 $cm^2 V^{-1} s^{-1}$, respectively, at 2.3 K.[19] Moreover, due to the extremely high carrier mobility, both the Quantum Hall effect (QHE) and Shubnikov-de Haas oscillations (SdH) can be observed at low temperature in single crystalline graphene.[20] Our graphene-on-Ge platform may offer a promising pathway to realize advanced electronics, optoelectronics, and photonics.[21,22]

2. Results and Discussion

2.1. Preparation of hBN/Graphene/hBN Sandwich Structure

In **Figure 1**a, wafer-scale single crystalline graphene has been grown at 916 °C on Ge(110) substrate using atmospheric-pressure CVD furnace in a methane gas environment.[2,23] More growth parameters are shown in Table S1 in the Supporting Information. The Raman spectra shown in Figure S1 (Supporting Information) suggest the synthesized graphene wafer possesses high crystalline quality and good uniformity. In Figure 1b-i, a piece of graphene/Ge(110) (1 × 1 cm^2) sample is cut from the wafer, and then a thin hBN flake with a thickness of ≈35 nm is mechanically applied to the graphene, and the corresponding SEM image of hBN/graphene/Ge(110) is shown in Figure 1c. Due to the extremely weak adhesion between graphene and the Ge(110), monolayer graphene can be peeled from Ge(110) substrate directly using the bilayer stack consisting of a slice of polyvinyl alcohol (PVA) and a larger slice of polydimethylsiloxane (PDMS), as shown in Figure 1b-ii. A SEM image of graphene-peeled Ge(110) substrate and an optical image of hBN/graphene on bilayer stack are shown in Figure 1d,e, respectively. Upon printing to another exfoliated hBN flake covered SiO_2 substrate, the sandwich of hBN/graphene/hBN is formed (Figure 1b-iii and iv) and an optical image is shown in Figure 1f. The formation process of hBN/graphene/hBN sandwich structure can

be monitored by Raman spectra, as displayed in Figure 1g. For hBN/graphene/hBN sandwich structure, the intensity ratio I_{2D}/I_G of graphene is the highest, which is due to the fact that encapsulated graphene by hBN is protected from external environment and the charge doping from substrate can been eliminated significantly.[24,25] Finally, using the edge-contact technique, Hall bar device is fabricated on hBN/graphene/hBN sandwich structure (Figure 1b-v) and the corresponding cross section transmission electron microscope (TEM) image is shown in Figure 1h. A certain slope of the edge formed in cross section ensures 1D edge contact between exposed graphene and metal lead because of lateral etching.[19] Compared with 2D surface contact interface, 1D edge contacts present no contaminations between graphene and metal. Therefore, electrons can travel freely between graphene and metal, ensuring better electrical conductivity.[19] In addition, a high-resolution cross-section STEM image (Figure 1i) from the red box in (h) reveals a clean interface between graphene and layered hBN, which reduces long-range and short-range scattering in graphene and thus increases carrier mobility.[26,27]

2.2. Raman Characterization of hBN/Graphene/hBN Sandwich Structure

Traditional wet-transferred graphene methods result in increased charge doping and strain fluctuations due to residual polymers and metal ions, which reduces the quality of the graphene crystal.[28] Using wet-transferred technology, the graphene grown on Ge(110) is wet-transferred on SiO_2 substrate and the crystal quality of graphene is evidenced by the extremely low $I_{D/G}$ (≈0.025) of D peak and G peak as shown in Figure S2a and S2b (Supporting Information).[29] However, the intensity ratio $I_{2D/G}$ of 2D peak and G peak in wet-transferred graphene can only reach ≈2.1 as shown in Figure S2c (Supporting Information). The low $I_{2D/G}$ originates from the dangling bonds of the SiO_2 substrate as well as the contamination-induced doping, which damages the ballistic transport of charge carriers.[24,30] Furthermore, the wet-transferred graphene shows an average hydrostatic strain ϵ as large as 0.18% in Figure S2d (Supporting Information) calculated as[31,32]

$$\epsilon = -\frac{1}{\omega_0}\frac{\Delta\omega_G}{\gamma} \quad (1)$$

where ω_0 is the G peak position at zero strain, $\Delta\omega_G$ is the frequency shift of the G peak, and γ is the Grüneisen parameter (slope of $\Delta\omega_{2D}/\Delta\omega_G$, where $\Delta\omega_{2D}$ is the frequency shift of the 2D peak), which is 2.2 in freestanding graphene. The unexpected strain fluctuations and charge doping seriously weaken the electrical properties of graphene by enhanced scattering effect and the all-dry transfer method will avoid these drawbacks.[33]

In the all-dry transfer case, the Raman characterization of hBN/graphene/hBN sandwich structure in Figure S3a (Supporting Information) shows a weak G peak at 1584 cm^{-1} and a strong 2D peaks at 2692 cm^{-1}, in which the $I_{2D/G}$ is as high as ≈7.6 in six Raman spectra as shown in **Figure 2**a (more details shown in Figure S3b,c, Supporting Information). The high $I_{2D/G}$ indicates that the graphene/hBN interface is free from charge doping induced by either substrate or external contaminations, thus facilitating more efficient charge transport through the clean interface.[29] Besides, the lack of D peak in sandwiched graphene suggests the all-dry transfer process is nondestructive. The charge doping and local strain induced by substrate together with the external contaminations will both seriously degrade the carrier transport in graphene. To qualitatively determine the dominant disorder source, the spatially resolved Raman spectra measurement in an area of 20 μm × 20 μm (red dashed box in Figure S3a, Supporting Information) is performed to obtain the position of the 2D peak (ω_{2D}) and G peak (ω_G). Using the vector-decomposition model, the relationship between ω_{2D} and ω_G in graphene is summarized in Figure 2b, where strain and charge doping are optically separated on the axis for strain (red dotted line) and doping (green dotted line).[31] Similar to the wet-transferred graphene, the slope ($\Delta\omega_{2D}/\Delta\omega_G$) of dry-transferred graphene is about 2.2 and parallel to the strain axis, suggesting that strain is the dominant disorder in both cases rather than charge doping. For cursory estimation of hydrostatic strain from G peak, the wet-transferred graphene on SiO_2 exhibits a red shift (namely, tensile strain) while dry-transferred graphene encapsulated in hBN tends to exhibit a blue shift (namely, compressive strain) and is closer to the freestanding point (black dot), indicating a smaller degree of strain inhomogeneity. In particular, the anomalous up shift of 2D peak in hBN/graphene/hBN sandwich structure can be attributed to the reduced electron–phonon coupling at high-symmetry point K caused by dielectric screening from thick hBN substrate, which is also known as the tuned Cohen anomaly.[34]

Following the formula (1) above, the exact value of the hydrostatic strain ϵ in dry-assembled graphene is extracted and summarized in Figure 2c, where the spatially resolved mapping of ϵ and its histogram are plotted. On the one hand, the all-dry transferred graphene manifests smaller average strain value (–0.05%) and distribution range (–0.2% to 0.1%) compared to wet-transferred graphene to SiO2 substrate (Figure S2d, Supporting Information). As a result, the strain-induced local pseudomagnetic fields in graphene is reduced and the corresponding intravalley scattering is suppressed, thus facilitating the more efficient movement of the carriers.[35,36] On the other hand, the all-dry transferred graphene illustrates a smaller random strain fluctuation which can be reflected by the full width at half maximum (FWHM) of the 2D peak (Γ_{2D}). In general, the reduced random strain variations can lead to a narrower 2D peak.[33] Extracted by Lorentz fitting, the Γ_{2D} of all-dry transferred graphene (Figure 2d) shows an average value of 18.8 cm^{-1}, which is much smaller than the value of 32.5 cm^{-1} for the wet-transferred graphene (Figure S2a, Supporting Information). It indicates the fact that the graphene transferred by the dry-assembled process exhibits less random strain fluctuations than that obtained by the wet transfer, which is conducive to improve the carrier mobility by the considerable suppression of scattering effects.

2.3. The Electrical Transport Measurements

The edge-contact Hall bar device is fabricated in the hBN/graphene/hBN sandwich structure as shown in the

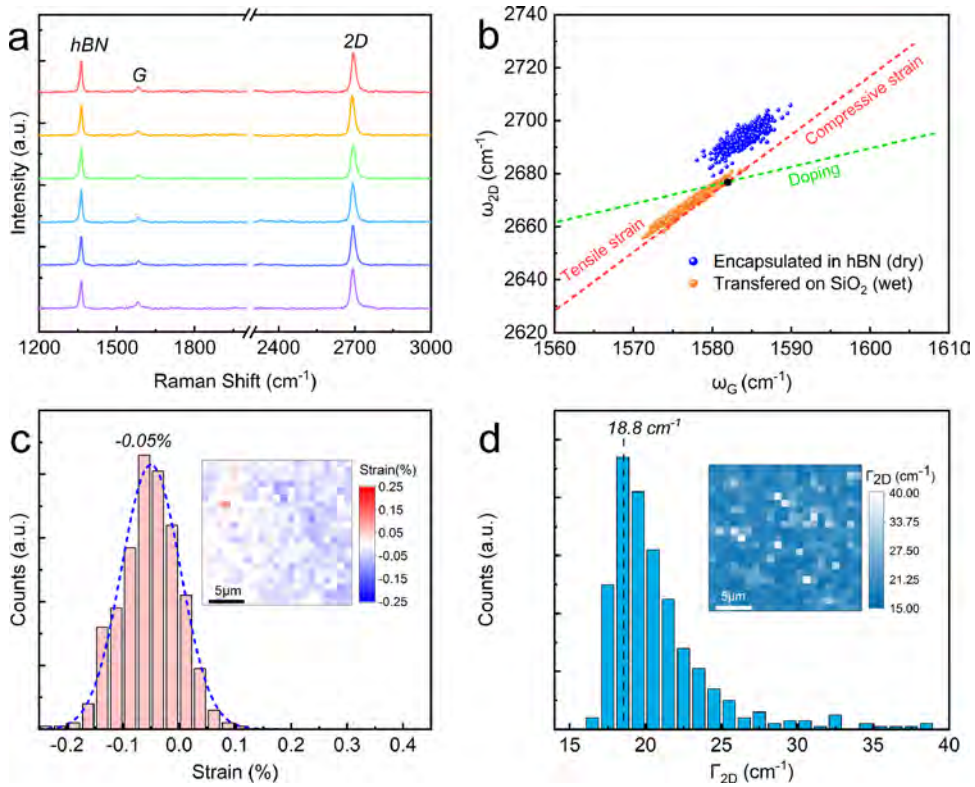

Figure 2. Raman characterization of hBN/graphene/hBN sandwich structure. a) Six typical Raman spectra of the sandwich structure (red dashed box in Figure S3a, Supporting Information). b) The relationship of the ω_{2D} and ω_G in the wet-transferred graphene on SiO_2 and dry-assembled sandwiched graphene. c) The histogram of strain obtained from an area of 20×20 μm^2. Inset: spatially resolved mapping of the strain. d) The histogram of the Γ_{2D} corresponding to c) with a maximum at 18.8 cm^{-1}. The inset shows the spatially resolved mapping of the Γ_{2D}.

inset of **Figure 3**a. To eliminate the influence of contact resistance, all electrical transports are performed by Kelvin four-terminal configuration at 2.3 K (pale blue) and 300 K (pink).[30] As a consequence of the linear dispersion relationship at the Dirac point of the graphene,[37] the four-terminal resistance R_{xx} (determined by V_{xx}/I as shown in the inset of Figure 3a) of Hall bar device exhibits a sharp peak as a function of back-gate voltage V_{bg}. The sharp peak, also known as the charge neutrality point (V_{CNP}), is located at −5 V, which manifests slight n doping existing due to the graphene-Cr work function difference.[19] Compared with the R_{xx} at 300 K, the low-temperature (2.3 K) resistance R_{xx} increases by a factor of 1.3 at V_{Dirac} due to the suppressed thermal activation. It should be noted that the high ratio of maximum resistance peak under low temperature and room temperature usually occurs in the disorder-suppressed monolayer graphene.[30]

The conductivity σ is determined by $\sigma = R_{xx}W/L$, where the W and L are width and length of device channel, respectively. By performing the Hall measurements with magnetic field $B =$ 0.25 T, the back-gate voltage dependent carrier density n can be calculated by dividing the $R_{xy}/B = 1/ne$ (details shown in Figure S4a, Supporting Information). The Hall resistance R_{xy} is obtained from V_{xy}/I as illustrated in the inset of Figure 3a. Afterward, the relationship between conductivity$\sigma$and charge carrier density n is shown in Figure 3b. At low carrier density ($n < 5 \times 10^{11}$ cm^{-2}), the low-temperature $\sigma - n$ curve is consistent with the linear Drude model,[38] but the self-consistent Boltzmann model fits the curve better at high carrier density, as demonstrated in Figure S4b (Supporting Information).[39] To extrapolate the disorder-induced charge carrier density fluctuations n^*, the relationship between log(σ) and log(n) is shown in Figure 3c.[36] The exact value of the n^* (guided by gray dashed line) is 3×10^{10} at 2.3 K and 9×10^{10} cm^{-2} at 300 K, respectively, which is much smaller than the wet-transferred graphene devices on SiO_2 substrate ($> 1 \times 10^{11}$ cm^{-2}).[38] This small fluctuation in carrier density is attributed to the reduction of doping- and strain-induced disorder during the dry transfer process, which coincides with the results of Raman characterization.[40]

According to mobility equation of $\epsilon_D = \sigma/ne$ from Drude model, the mobility ϵ_D as a function of the charge carrier density n is plotted in Figure 3d. Near the charge neutrality point at 2.3 K, the maximum mobilities of electrons (ϵ_e) and holes (ϵ_h) are 9.6×10^4 and 1.0×10^5 cm^2 V^{-1} s^{-1}, respectively. The carrier mobility can also be estimated from the linear fitting near Dirac point in Figure S4b (Supporting Information), and the maximum mobilities of electrons and holes are 8.3×10^4 and 11.5×10^4 cm^2 V^{-1} s^{-1}, respectively, which are approximate to the values mentioned earlier. Furthermore, as the temperature is elevated to room temperature (300 K), the maximum mobilities of electrons (ϵ_e) and holes (ϵ_h) change to 4.6×10^4 and 6.0×10^4 cm^2 V^{-1} s^{-1}, respectively. Our study suggests that the edge-contact Hall bar device built on hBN/graphene/hBN sandwich structure provides an unique architecture to acquire the accurate mobility of 2D materials, and the estimated carrier mobility of single

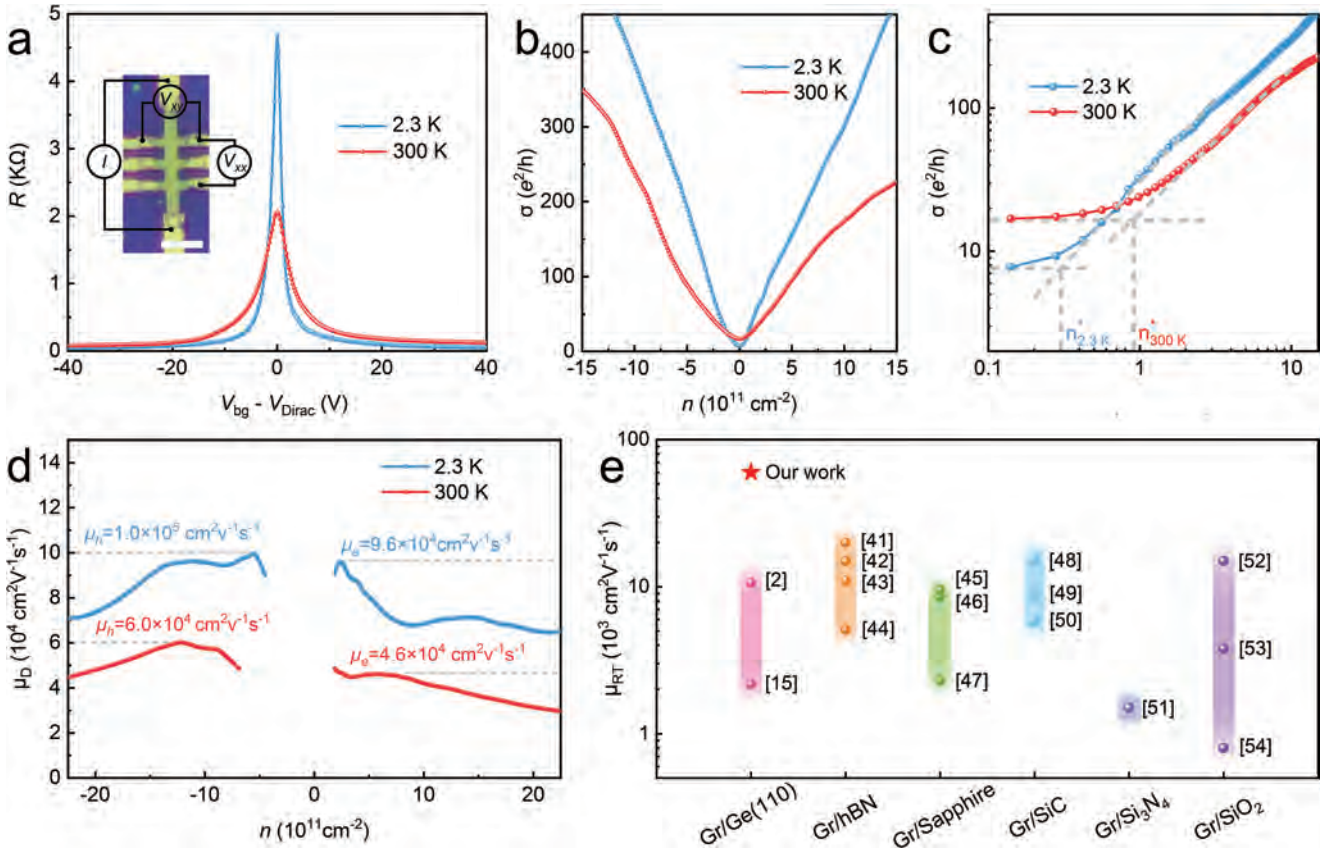

Figure 3. Transport characterization of an edge-contact Hall bar device. a) Typical transfer curves of a Hall bar device at 2.3 K (pale blue) and 300 K (pink). Inset: optical image of the Hall bar device and the scale bar is 5 μm. b) The relationship of conductance σ and carrier density n of the device extracted from (a). c) The charge carrier density fluctuations n^* extracted from the double-logarithmic scale of b) at 2.3 and 300 K. d) Density-dependent carrier mobilities $\epsilon_D$of the hBN/graphene/hBN sandwich structure extracted by Drude model according to the formula: $\epsilon_D = \sigma/ne$, with the density of charge carriers n obtained through the Hall measurements (details shown in Figure S4a, Supporting Information). e) Comparison of carrier mobilities of graphene grown on Ge(110) with that of graphene grown on other nonmetal substrates.

crystalline graphene grown on Ge(110) is found to be much higher than those prepared on other nonmetallic substrates (semiconductors or insulators) including sapphire, SiO_2, hBN, SiC, and Si_3N_4 as shown in Figure 3e.[2,15,41–54]

The ultrahigh mobility found in the edge-contact Hall bar device built on hBN/graphene/hBN sandwich structure is further verified by other four parallel devices, as depicted in Figure S5 in the Supporting Information. For other four devices, the mobilities obtained at 2.3 K are distributed in the range of 4.5×10^4–7.7×10^4 cm^2 V^{-1} s^{-1}. And, the corresponding carrier density fluctuations n^* vary from 6.3×10^{10} to 3.7×10^{10} cm^{-2} as show in Figure S6 (Supporting Information).

2.4. The QHE and SdH Oscillations

The ultrahigh carrier mobility enables the observation of novel physical phenomena in the edge-contact Hall bar device, including half-inter QHE and SdH oscillations, as shown in **Figure 4**. Below a fixed back-gate voltage V_{bg} = 35 V, the well-defined plateaux of Hall resistance R_{xy}(blue) and the oscillatory longitudinal magnetoresistance R_{xx} (red) are observed, as shown in Figure 4a. The quantized conductance (R_{xy}^{-1}) of plateaux in Figure 4a are in accordance with the following formula[20]

$$R_{xy}^{-1} = \pm g_s (n + 1/2) e^2/h \quad (2)$$

where g_s is the degeneracy of the Landau level of graphene (equal to four), ± represents the electrons and holes, respectively, n is an integer, e represents the elementary charge, and h is the Planck constant. With a back-gate voltage V_{bg} = 35 V, the filling factors $\nu = \pm g_s(n + 1/2) = 10, 14, 18...$ (denoted as black dashed line) are observed. Decreasing the back-gate voltage V_{bg} to 5 V, the lower filling factors ν = 2, 6, 10 are observed as displayed in inset of Figure 4a. In integer quantum Hall states, the oscillations of magnetoresistance R_{xx} occur when the quantization Hall resistance R_{xy} appears, which is well described by

$$\Delta R_{xx} = R(B, T) \cos\left[2\pi \left(B_F/B + 1/2 + \beta\right)\right] \quad (3)$$

where $R(B,T)$ is the amplitude of the SdH oscillations, B_F is the frequency of the oscillations, and β is the Berry's phase of graphene.[20] The magnetoresistance show more SdH oscillations due to the increased Landau level density of states (DOS) at high carrier density. An increased back-gate voltage of 45 V leads to more Landau levels being occupied by electrons, as

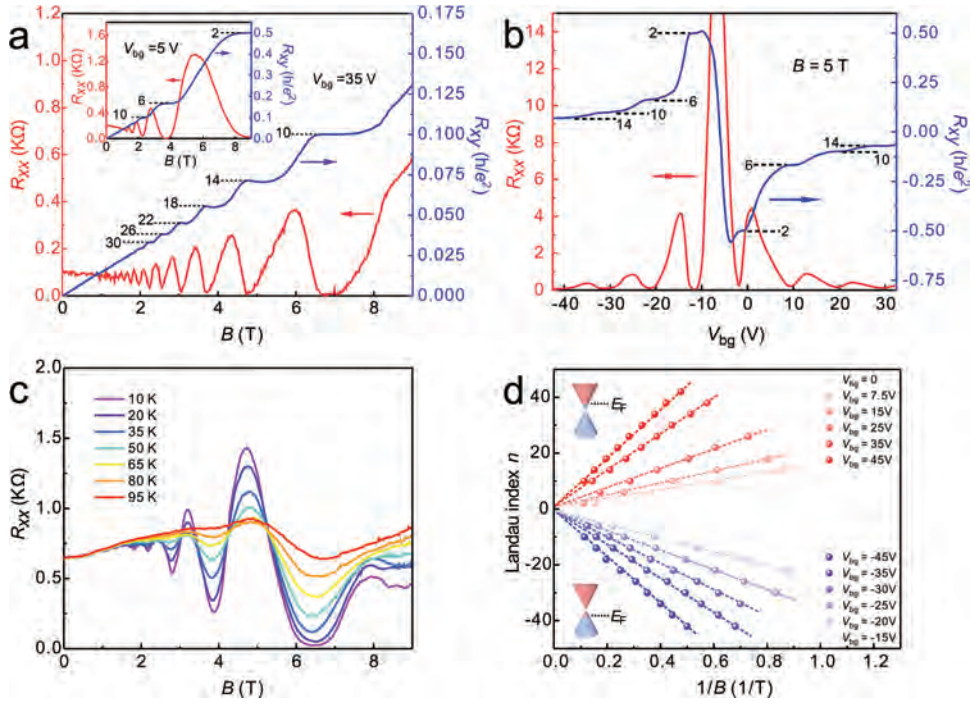

Figure 4. QHE and SdH oscillations of an edge-contact Hall bar device. a) Hall resistance R_{xy} (blue) and magnetoresistance R_{xx} (red) as a function of vertical magnetic field B at 2.3 K with a back-gate voltage V_{bg} at 35 and 5 V (inset). Well-defined Quantum Hall plateaux with the quantized filling factors $\nu = 2, 6, 10, 14...$ and SdH oscillations are observed. b) The QHE and SdH oscillations as a function of back-gate voltage V_{bg} at fixed magnetic field $B =$ 5 T, which measured at 2.3 K. c) The robustness of magneto-oscillations to temperature dependence from 10 to 95 K ($V_{bg} = 0$). d) The fan diagram of SdH oscillations for different V_{bg}. The Landau index n of the magnetoresistance R_{xx} as a function of $1/B$ is almost symmetrical, which corresponds to the electron–hole symmetry existing in graphene.

shown in Figure S7 (Supporting Information), confirming the enhanced electron–electron interactions by the observation of the fractional quantum Hall effect.[55] Both quantum Hall effect and the SdH oscillations provide a convincing evidence for the existence of extremely high mobility in the edge-contact Hall bar device built on hBN/graphene/hBN sandwich structure, in which the single crystalline graphene is initially grown on Ge(110) substate.

The QHE and SdH oscillations are observed for both electrons and holes by altering the V_{bg} across the Dirac point with a fixed magnetic field B (5 T). In the case of electrons ($V_{bg} - V_{CNP} > 0$) or holes ($V_{bg} - V_{CNP} < 0$) filling Landau levels, the quantum Hall plateaux (blue) and symmetric SdH oscillations (red) occur synchronously, as shown in Figure 4b, in which the plateaux of the Hall resistance are denoted by black dashed line.

Meanwhile, the ultrahigh mobility in graphene can also be proved by the robustness of the magneto-oscillations to temperature dependence.[56] The magnetic oscillation curves under variable temperature are shown in Figure 4c, where the SdH oscillations gradually weaken with increasing temperature, and disappear when the temperature approaches 100 K. The SdH oscillations are able to preserve over a wide temperature range, indicating the strong robustness of carrier transport to external thermal fluctuations, which can be further utilized in quantized Hall resistance (QHR) applications.[57]

Arising from the symmetric band structure of graphene,[37] Landau levels in the quantum Hall regime can be filled by both electrons or holes. Hence, the relationship of Landau index n (nth minimum R_{xx}) and $1/B$ are plotted in the fan diagram in Figure 4d. At different back-gate voltages, the nonzero intercept of linear fit to the data with Landau index n and $1/B$ symmetrically converge on both sides of the n-index axis. The dry transfer of graphene assisted with hBN offers an appropriate method to explore the inherent carrier mobility of graphene grown on Ge(110) substrate. The SdH oscillations over a wide range of back-gate voltages once again prove the extremely high intrinsic carrier mobility of CVD graphene, which sets a solid foundation for the applications of nonmetal grown graphene.

3. Conclusion

In summary, the advanced dry-transferred method together with the edge-contact technique are developed to pick up the graphene directly from Ge(110) substrate, and form high quality Hall bar device built on hBN/graphene/hBN sandwich structure. The transport measurements of Hall bar device in both low temperature and room temperature demonstrate that the graphene grown on Ge(110) possess extremely high carrier mobility, which is further verified by the observation of the well-defined QHE and SdH oscillations. The superiority of the mobility in graphene grown on Ge(110) may open an avenue to drive the semiconductor process-compatible nonmetal graphene toward more promising applications.

4. Experimental Section

Dry Transfer Process: First, PVA film was prepared by dropping PVA solution (8%) on the glass slide and dried it in the atmosphere. Then a piece of polydimethylsiloxane (PDMS, 1×1 cm^2) block was attached on the glass slide, and the prepared PVA film was cut to 2 × 2 mm in size and placed on PDMS to form a stack of PVA/PDMS film. Prior to the transfer of graphene, the hBN flakes with a thickness of around 30–40 nm was mechanically exfoliated on the surface of the graphene. With the optical examination, the polymer stack was positioned in a micromanipulator. With a slight horizontal inclination, the stack was dropped down at the desired position. Afterward, the sample was heated to 75 °C at first and the stack was brought into mechanical contact with the hBN/graphene on Ge substrate from one side slowly. When the PVA film completely covered the hBN/graphene, the temperature of sample continued to be kept at 75 °C for 3 min and then cooled down to room temperature. Rapidly, the graphene was picked up from the Ge substrate and optical examination was performed before the graphene/hBN/PVA/PDMS stack was transferred to another exfoliated hBN flake on SiO_2 substrate. At 80 °C, PVA and PDMS could be easily separated due to the weak adhesion between them while the graphene/hBN hybrid would be released to another slice of hBN.

Device Fabrication: The edge-contact Hall bar device fabrication consists of two key steps, namely, the exposure of the edge of the encapsulated graphene layer and the deposition of metal electrodes. To define the shape of Hall bar device, a poly(methyl methacrylate) (PMMA) film was spin coated as a mask and then the electron beam lithography (EBL, Zeiss Sigma system) was used to pattern the PMMA layer to define the device shape. Afterward the hBN/graphene/hBN stack was etched in an RIE system with a mixture of O_2 (4 sccm) and CHF_3 (40 sccm) gases under 60 W at a pressure of 10 Pa. The PMMA layer with acetone was dissolved. Afterward, the Methyl methacrylate (MMA) and PMMA layers were spin coated, respectively, before the EBL process. Developing immediately after EBL process, 10 nm Cr and 80 nm Au were deposited to form the electrical contact between Cr/Au electrodes and graphene by electron beam evaporation (EBE) system. After the lift-off process, the devices were annealed in ambient pressure with a mixture of Ar (200 sccm) and H_2 (20 sccm) at 250 °C for 3 h to remove residual polymer.

Raman Measurement: The Raman spectra of hBN/graphene/hBN sandwich structure was measured using a micro-Raman spectroscope (HR800, Horiba) in ambient environment. In order to eliminate the parasitic thermal effects and guarantee the signal-to-noise ratio, the power of laser with a wavelength of 514 nm was set to the minimum value of 5 mW. The diameter of laser spot is about 1 µm.

Transport Measurement: The transport measurement was performed by a physical property measurement system (PPMS-9T, Quantum Design) from 2.3 to 300 K. In order to apply a back-gate voltage to alter the carrier density of the graphene in Hall device, an external Keithley 2400 SourceMeter was utilized.

Supporting Information

Supporting Information is available from the Wiley Online Library or from the author.

Acknowledgements

The authors thank National Natural Science Foundation of China (Grant Nos. 51925208, 61974157, and 62122082), National Key R&D Program of China (Grant Nos. 2022YFB3204800 and 2022YFB4400100), Strategic Priority Research Program (B) of the Chinese Academy of Sciences (No. XDB30030000), Science and Technology Commission of Shanghai Municipality (No. 21JC1406100). Some of the experiments were carried out at the Fudan nanofabrication Laboratory.

Conflict of Interest

The authors declare no conflict of interest.

Data Availability Statement

The data that support the findings of this study are available from the corresponding author upon reasonable request.

Keywords

chemical vapor decomposition graphene, dry transfer, electrical transport, Ge(110), hexagonal boron nitride, quantum Hall effect, Raman

Received: June 11, 2023
Revised: December 12, 2012
Published online: July 19, 2023

[1] G. Wang, M. Zhang, Y. Zhu, G. Q. Ding, D. Jiang, Q. L. Guo, S. Liu, X. M. Xie, P. K. Chu, Z. F. Di, X. Wang, *Sci. Rep.* **2013**, *3*, 6.
[2] J. H. Lee, E. K. Lee, W. J. Joo, Y. Jang, B. S. Kim, J. Y. Lim, S. H. Choi, S. J. Ahn, J. R. Ahn, M. H. Park, C. W. Yang, B. L. Choi, S. W. Hwang, D. Whang, *Science* **2014**, *344*, 286.
[3] J. S. Moon, D. Curtis, M. Hu, D. Wong, C. McGuire, P. M. Campbell, G. Jernigan, J. L. Tedesco, B. VanMil, R. Myers-Ward, C. Eddy, D. K. Gaskill, *IEEE Electron Device Lett.* **2009**, *30*, 650.
[4] H. Wang, A. Hsu, J. Wu, J. Kong, T. Palacios, *IEEE Electron Device Lett.* **2010**, *31*, 906.
[5] E. C. Ahn, *npj 2D Mater. Appl.* **2020**, *4*, 14.
[6] X. Y. Lin, W. Yang, K. L. Wang, W. S. Zhao, *Nat. Electron.* **2019**, *2*, 274.
[7] H. Agarwal, B. Terres, L. Orsini, A. Montanaro, V. Sorianello, M. Pantouvaki, K. Watanabe, T. Taniguchi, D. Van Thourhout, M. Romagnoli, F. H. L. Koppens, *Nat. Commun.* **2021**, *12*, 6.
[8] L. Lin, J. C. Zhang, H. S. Su, J. Y. Li, L. Z. Sun, Z. H. Wang, F. Xu, C. Liu, S. Lopatin, Y. H. Zhu, K. C. Jia, S. L. Chen, D. R. Rui, J. Y. Sun, R. W. Xue, P. Gao, N. Kang, Y. Han, H. Q. Xu, Y. Cao, K. S. Novoselov, Z. Q. Tian, B. Ren, H. L. Peng, Z. F. Liu, *Nat. Commun.* **2019**, *10*, 7.
[9] T. R. Wu, X. F. Zhang, Q. H. Yuan, J. C. Xue, G. Y. Lu, Z. H. Liu, H. S. Wang, H. M. Wang, F. Ding, Q. K. Yu, X. M. Xie, M. H. Jiang, *Nat. Mater.* **2016**, *15*, 43.
[10] D. Neumaier, S. Pindl, M. C. Lemme, *Nat. Mater.* **2019**, *18*, 525.
[11] T. B. Wang, P. L. Li, X. D. Hu, M. Gao, Z. F. Di, Z. Y. Xue, M. Zhang, *Appl. Surf. Sci.* **2020**, *529*, 8.
[12] P. L. Li, W. Y. Wei, M. Zhang, Y. F. Mei, P. K. Chu, X. M. Xie, Q. H. Yuan, Z. F. Di, *Nano Today* **2020**, *34*, 100908.
[13] B. Kiraly, R. M. Jacobberger, A. J. Mannix, G. P. Campbell, M. J. Bedzyk, M. S. Arnold, M. C. Hersam, N. P. Guisinger, *Nano Lett.* **2015**, *15*, 7414.
[14] J. Grzonka, I. Pasternak, P. P. Michalowski, V. Kolkovsky, W. Strupinski, *Appl. Surf. Sci.* **2018**, *447*, 582.
[15] S. J. Yang, S. Choi, F. O. O. Ngome, K. J. Kim, S. Y. Choi, C. J. Kim, *Nano Lett.* **2019**, *19*, 3590.
[16] A. S. Mayorov, R. V. Gorbachev, S. V. Morozov, L. Britnell, R. Jalil, L. A. Ponomarenko, P. Blake, K. S. Novoselov, K. Watanabe, T. Taniguchi, A. K. Geim, *Nano Lett.* **2011**, *11*, 2396.
[17] C. R. Dean, A. F. Young, I. Meric, C. Lee, L. Wang, S. Sorgenfrei, K. Watanabe, T. Taniguchi, P. Kim, K. L. Shepard, J. Hone, *Nat. Nanotechnol.* **2010**, *5*, 722.
[18] Q. Z. Li, E. H. Hwang, S. D. Sarma, *Phys. Rev. B* **2011**, *84*, 16.
[19] L. Wang, I. Meric, P. Y. Huang, Q. Gao, Y. Gao, H. Tran, T. Taniguchi, K. Watanabe, L. M. Campos, D. A. Muller, J. Guo, P. Kim, J. Hone, K. L. Shepard, C. R. Dean, *Science* **2013**, *342*, 614.
[20] Y. B. Zhang, Y. W. Tan, H. L. Stormer, P. Kim, *Nature* **2005**, *438*, 201.
[21] M. Romagnoli, V. Sorianello, M. Midrio, F. H. L. Koppens, C. Huyghebaert, D. Neumaier, P. Galli, W. Templ, A. D'Errico, A. C. Ferrari, *Nat. Rev. Mater.* **2018**, *3*, 392.

[22] D. Akinwande, C. Huyghebaert, C. H. Wang, M. I. Serna, S. Goossens, L. J. Li, H. S. P. Wong, F. H. L. Koppens, *Nature* **2019**, *573*, 507.
[23] J. Y. Dai, D. X. Wang, M. Zhang, T. C. Niu, A. Li, M. Ye, S. Qiao, G. Q. Ding, X. M. Xie, Y. Q. Wang, P. K. Chu, Q. H. Yuan, Z. F. Di, X. Wang, F. Ding, B. I. Yakobson, *Nano Lett.* **2016**, *16*, 3160.
[24] M. Kalbac, A. Reina-Cecco, H. Farhat, J. Kong, L. Kavan, M. S. Dresselhaus, *ACS Nano* **2010**, *4*, 6055.
[25] C. Casiraghi, S. Pisana, K. S. Novoselov, A. K. Geim, A. C. Ferrari, *Appl. Phys. Lett.* **2007**, *91*, 233108.
[26] Z. J. Huang, E. Cuniberto, S. Park, K. Kisslinger, Q. Wu, T. Taniguchi, K. Watanabe, K. G. Yager, D. Shahrjerdi, *Small* **2022**, *18*, 12.
[27] N. Leconte, H. Kim, H. J. Kim, D. H. Ha, K. Watanabe, T. Taniguchi, J. Jung, S. Jung, *Nanoscale* **2017**, *9*, 6041.
[28] H. P. Wang, G. Yu, *Adv. Mater.* **2016**, *28*, 4956.
[29] L. Banszerus, M. Schmitz, S. Engels, J. Dauber, M. Oellers, F. Haupt, K. Watanabe, T. Taniguchi, B. Beschoten, C. Stampfer, *Sci. Adv.* **2015**, *1*, 6.
[30] P. Blake, R. Yang, S. V. Morozov, F. Schedin, L. A. Ponomarenko, A. A. Zhukov, R. R. Nair, I. V. Grigorieva, K. S. Novoselov, A. K. Geim, *Solid State Commun.* **2009**, *149*, 1068.
[31] J. E. Lee, G. Ahn, J. Shim, Y. S. Lee, S. Ryu, *Nat. Commun.* **2012**, *3*, 8.
[32] T. M. G. Mohiuddin, A. Lombardo, R. R. Nair, A. Bonetti, G. Savini, R. Jalil, N. Bonini, D. M. Basko, C. Galiotis, N. Marzari, K. S. Novoselov, A. K. Geim, A. C. Ferrari, *Phys. Rev. B* **2009**, *79*, 8.
[33] C. Neumann, S. Reichardt, P. Venezuela, M. Drogeler, L. Banszerus, M. Schmitz, K. Watanabe, T. Taniguchi, F. Mauri, B. Beschoten, S. V. Rotkin, C. Stampfer, *Nat. Commun.* **2015**, *6*, 7.
[34] F. Forster, A. Molina-Sanchez, S. Engels, A. Epping, K. Watanabe, T. Taniguchi, L. Wirtz, C. Stampfer, *Phys. Rev. B* **2013**, *88*, 7.
[35] N. Levy, S. A. Burke, K. L. Meaker, M. Panlasigui, A. Zettl, F. Guinea, A. H. C. Neto, M. F. Crommie, *Science* **2010**, *329*, 544.
[36] N. J. G. Couto, D. Costanzo, S. Engels, D. K. Ki, K. Watanabe, T. Taniguchi, C. Stampfer, F. Guinea, A. F. Morpurgo, *Phys. Rev. X* **2014**, *4*, 13.
[37] K. S. Novoselov, A. K. Geim, S. V. Morozov, D. Jiang, M. I. Katsnelson, I. V. Grigorieva, S. V. Dubonos, A. A. Firsov, *Nature* **2005**, *438*, 197.
[38] D. De Fazio, D. G. Purdie, A. K. Ott, P. Braeuninger-Weimer, T. Khodkov, S. Goossens, T. Taniguchi, K. Watanabe, P. Livreri, F. H. L. Koppens, S. Hofmann, I. Goykhman, A. C. Ferrari, A. Lombardo, *ACS Nano* **2019**, *13*, 8926.
[39] N. Petrone, C. R. Dean, I. Meric, A. M. van der Zande, P. Y. Huang, L. Wang, D. Muller, K. L. Shepard, J. Hone, *Nano Lett.* **2012**, *12*, 2751.
[40] J. M. Xue, J. Sanchez-Yamagishi, D. Bulmash, P. Jacquod, A. Deshpande, K. Watanabe, T. Taniguchi, P. Jarillo-Herrero, B. J. Leroy, *Nat. Mater.* **2011**, *10*, 282.
[41] S. J. Tang, H. M. Wang, H. S. Wang, Q. J. Sun, X. Y. Zhang, C. X. Cong, H. Xie, X. Y. Liu, X. H. Zhou, F. Q. Huang, X. S. Chen, T. Yu, F. Ding, X. M. Xie, M. H. Jiang, *Nat. Commun.* **2015**, *6*, 7.
[42] T. Gao, X. J. Song, H. W. Du, Y. F. Nie, Y. B. Chen, Q. Q. Ji, J. Y. Sun, Y. L. Yang, Y. F. Zhang, Z. F. Liu, *Nat. Commun.* **2015**, *6*, 8.
[43] X. J. Song, T. Gan, Y. F. Nie, J. N. Zhuang, J. Y. Sun, D. L. Ma, J. P. Shi, Y. W. Lin, F. Ding, Y. F. Zhang, Z. F. Liu, *Nano Lett.* **2016**, *16*, 6109.
[44] L. X. Chen, H. M. Wang, S. J. Tang, L. He, H. S. Wang, X. J. Wang, H. Xie, T. R. Wu, H. Xia, T. X. Li, X. M. Xie, *Nanoscale* **2017**, *9*, 11475.
[45] Z. L. Chen, C. Y. Xie, W. D. Wang, J. P. Zhao, B. Y. Liu, J. Y. Shan, X. Y. Wang, M. Hong, L. Lin, L. Huang, X. Lin, S. Y. Yang, X. Gao, Y. F. Zhang, P. Gao, K. S. Novoselov, J. Y. Sun, Z. F. Liu, *Sci. Adv.* **2021**, *7*, 7.
[46] J. Z. Li, M. G. Chen, A. Samad, H. C. Dong, A. Ray, J. W. Zhang, X. C. Jiang, U. Schwingenschlogl, J. Domke, C. L. Chen, Y. Han, T. Fritz, R. S. Ruoff, B. Tian, X. X. Zhang, *Nat. Mater.* **2022**, *21*, 740.
[47] N. Mishra, S. Forti, F. Fabbri, L. Martini, C. McAleese, B. Conran, P. R. Whelan, A. Shivayogimath, B. S. Jessen, L. Buss, J. Falta, I. Aliaj, S. Roddaro, J. I. Flege, P. Boggild, K. B. K. Teo, C. Coletti, *Small* **2019**, *15*, 8.
[48] Q. B. Liu, C. Yu, Z. Z. He, G. D. Gu, J. J. Wang, C. J. Zhou, J. C. Guo, X. D. Gao, Z. H. Feng, *Appl. Surf. Sci.* **2018**, *454*, 68.
[49] X. S. Wu, Y. K. Hu, M. Ruan, N. K. Madiomanana, J. Hankinson, M. Sprinkle, C. Berger, W. A. de Heer, *Appl. Phys. Lett.* **2009**, *95*, 3.
[50] J. L. Tedesco, B. L. VanMil, R. L. Myers-Ward, J. M. McCrate, S. A. Kitt, P. M. Campbell, G. G. Jernigan, J. C. Culbertson, C. R. Eddy, D. K. Gaskill, *Appl. Phys. Lett.* **2009**, *95*, 122102.
[51] J. Y. Chen, Y. L. Guo, Y. G. Wen, L. P. Huang, Y. Z. Xue, D. C. Geng, B. Wu, B. R. Luo, G. Yu, Y. Q. Liu, *Adv. Mater.* **2013**, *25*, 992.
[52] H. N. Ci, J. T. Chen, H. Ma, X. L. Sun, X. Y. Jiang, K. C. Liu, J. Y. Shan, X. Y. Lian, B. Jiang, R. J. Liu, B. Z. Liu, G. Q. Yang, W. J. Yin, W. Zhao, L. Z. Huang, T. Gao, J. Y. Sun, Z. F. Liu, *Adv. Mater.* **2022**, *34*, 2206389.
[53] H. P. Wang, X. D. Xue, Q. Q. Jiang, Y. L. Wang, D. C. Geng, L. Cai, L. P. Wang, Z. P. Xu, G. Yu, *J. Am. Chem. Soc.* **2019**, *141*, 11004.
[54] H. Kim, I. Song, C. Park, M. Son, M. Hong, Y. Kim, J. S. Kim, H. J. Shin, J. Baik, H. C. Choi, *ACS Nano* **2013**, *7*, 6575.
[55] K. I. Bolotin, F. Ghahari, M. D. Shulman, H. L. Stormer, P. Kim, *Nature* **2009**, *462*, 196.
[56] A. J. M. Giesbers, U. Zeitler, M. I. Katsnelson, L. A. Ponomarenko, T. M. Mohiuddin, J. C. Maan, *Phys. Rev. Lett.* **2007**, *99*, 4.
[57] R. Ribeiro-Palau, F. Lafont, J. Brun-Picard, D. Kazazis, A. Michon, F. Cheynis, O. Couturaud, C. Consejo, B. Jouault, W. Poirier, F. Schopfer, *Nat. Nanotechnol.* **2015**, *10*, 965.

ADVANCED MATERIALS INTERFACES
Open Access

Supporting Information

for *Adv. Mater. Interfaces*, DOI 10.1002/admi.202300482

Extremely High Intrinsic Carrier Mobility and Quantum Hall Effect Of Single Crystalline Graphene Grown on Ge(110)

Wang Guo, Miao Zhang, Zhongying Xue, Paul K. Chu, Yongfeng Mei, Ziao Tian and Zengfeng Di**

WILEY-VCH

Supporting Information

Extremely high intrinsic carrier mobility and quantum Hall effect of single crystalline graphene grown on Ge(110)

Wang Guo[1,2], Miao Zhang[1], Zhongying Xue[1], Paul K. Chu[3], Yongfeng Mei[4], Ziao Tian[1*], and Zengfeng Di[1*]

[1] State Key Laboratory of Functional Materials for Informatics, Shanghai Institute of Microsystem and Information Technology, Chinese Academy of Sciences, Shanghai 200050, China.

[2] Center of Materials Science and Optoelectronics Engineering, University of Chinese Academy of Sciences, Beijing 100049, China.

[3]Department of Physics, Department of Materials Science and Engineering, and Department of Biomedical Engineering, City University of Hong Kong, Tat Chee Avenue, Kowloon, Hong Kong, China

[4]Department of Materials Science, Fudan University, Shanghai 200433, China

* email: zatian@mail.sim.ac.cn (Z.A.Tian); zfdi@mail.sim.ac.cn (Z.F.Di)

Supporting Section 1: Chemical vapor deposition of graphene on Ge(110) substrate

Table S1 The growth parameters.

Stage	Time (min)	Ar	H_2	CH_4	Temperature (°C)
Ramping stage	120min	300	30	0	916
Growth stage	20min	350	35	1.6	916
	660min	700	70	0.8	916
	60min	700	70	2.0	916
Cooling stage	60min	700	70	0	60

The Raman and AFM results are shown in Figure S1. The Raman spectra of nine representative regions across the wafer (Figure S1a) show a lack of D peak and high $I_{2D/G}$ (≈2), indicating satisfactory crystal quality and uniformity of graphene, as shown in Figure S1b. AFM image in Figure S1c shows the presence of wrinkles caused by the mismatch between the thermal expansion coefficients of the graphene and Ge substrates. Nanoscale height steps and particle-free surface of the as-grown graphene facilitate the ensuing dry transfer process.

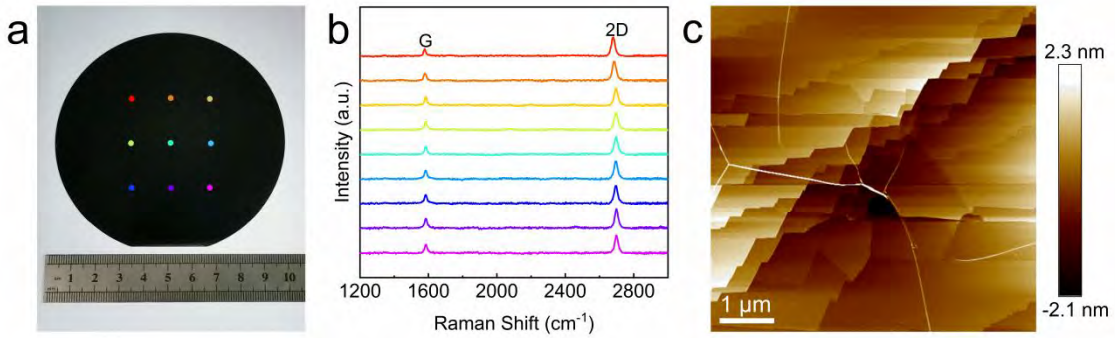

Figure S1. Wafer-scale graphene grown on Ge(110) by chemical vapor deposition (CVD). a) The optical image of 4-inch wafer-scale graphene on Ge(110) substrate. b) The Raman spectra of the graphene corresponding to the 9 colored points in (a). c) The AFM image of graphene/Ge(110).

Supporting Section 2: Wet transfer of as-grown graphene on SiO_2 substrate.

The graphene/Ge(110) wafer is cut into 1 × 1 cm slice after growth process, and then poly(methyl methacrylate) (PMMA, 4%) solution is spin-coated on the slice with a rotational speed of 4000 r/min. Afterwards, the graphene/Ge(110) slice is placed on a hot plate at 130°C for 8 min, followed by etching away the Ge substrate using a mixture of DI water: H_2O_2 : HF = 10 : 1 : 1. After corrosion, the graphene/PMMA film is fished out with hydrophilic substrate and then placed in deionized water so as to wash away the residual corrosion liquid. The film is then transferred on a SiO_2/Si substrate and after the graphene/PMMA film naturally adhered to the substrate completely, the sample is heated at 75 ℃ for 10 min. Finally, the PMMA film is dissolved in acetone and the residual solvent is washed with isopropanol (IPA).

Before Raman measurement, the sample is heated at 100 ℃ for 5 min to remove the absorbed air and water. In Figure S2a, a typical Raman spectrum of the optical image in inset shows a full width at half maximum (FWHM) of the 2D peak, $\Gamma_{2D} \approx$ 32.5 cm^{-1}, comparable to the reported values of the graphene grown on copper.[1] To further estimate the crystal quality of the graphene transferred on SiO_2 substrate, the intensity ratios $I_{D/G}$ for D peak and G peak and $I_{2D/G}$ for 2D peak and G peak are investigated in Figure S2b and Figure S2c respectively. In the area of 15 μm × 15 μm, the average $I_{D/G}$ values as low as ~0.025 are similar to those reported in single-crystal CVD graphene grown on copper, implying few defects existing in graphene.[2] Meanwhile, due to the sensitivity of 2D peak intensity to charge doping, the substrate and contamination-induced low $I_{2D/G}$ value (~2.1) is inevitable. Nonetheless, the narrowly distributed $I_{2D/G}$ values also demonstrate that the graphene grown on Ge(110) substrate show satisfactory homogeneity.

In order to further probe the local strain of the graphene transferred onto SiO_2 substrate, the hydrostatic strain ε is calculated fallowing the formula (1) as mentioned in the main text. The corresponding spatially resolved mapping (inset) and its histogram are plotted in Figure S2d. Despite weak D peak and the uniformity of $I_{2D/G}$, the random fluctuations of compress strain (inset) show strong non-uniformity.

Overall, the strain in the whole area displays an average value of 0.18% and ranges from -0.1% to 0.35%, which is much larger than the dry-assembled graphene discussed in the main text. The appreciable random strain variations can be mostly attributed to the wet-transfer method. Besides, the dangling bonds of the SiO_2 substrate tend to induce non-negligible charge doping and form long-range potential fluctuations. As a result, the transport of carriers will be seriously hindered, leading to the degradation of mobility.

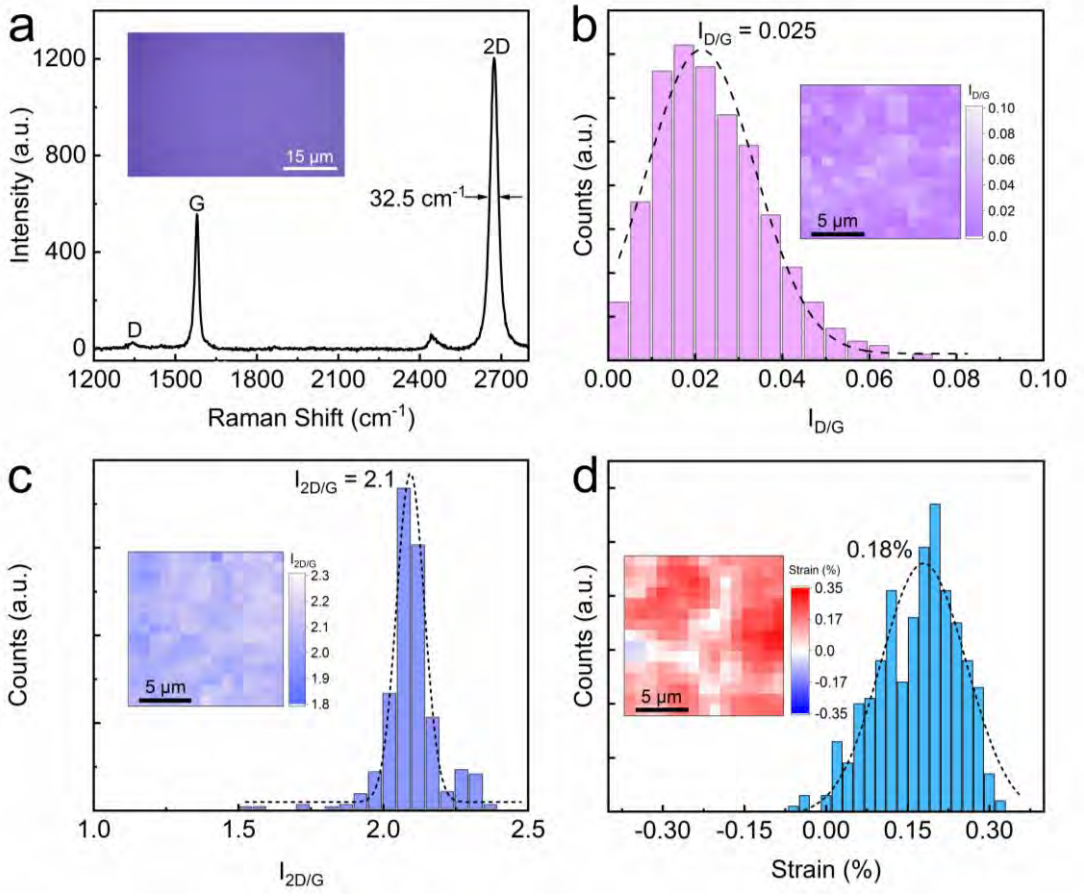

Figure S2. Raman Characteristics of the graphene transferred on SiO_2 Substrate. a) A typical Raman spectrum of the as-transferred graphene using the wet etching technique is shown in the optical image of the inset. b) Histogram and mapping of the intensity ratio $I_{D/G}$ of D peaks and G peaks. c) Histogram and spatially resolved mapping of the intensity ratio $I_{2D/G}$ of 2D peaks and G peaks. d) Histogram and spatially resolved mapping of the strain.

Supporting Section 3: The analysis of intensity ratio $I_{2D/G}$ of 2D peak and G peak

The Raman characterization of the hBN-encapsulated graphene in Figure 2 of the main text is performed in the area of the red dashed box in Figure S3a. The corresponding spatially resolved mapping and statistical histogram of intensity ratio $I_{2D/G}$ of 2D peak and G peak are illustrated in Figure S3b and Figure S3c respectively. Because the intensity of 2D peak in graphene is susceptible to charge doping, while higher $I_{2D/G}$ often represents smaller potential inhomogeneity and is conducive for high-performance devices.[3] In hBN-encapsulated graphene, the average value of $I_{2D/G}$ lies at 7.65 and only a small percentage of the $I_{2D/G}$ are less than 5. The lower $I_{2D/G}$ can be attributed to the presence of contamination-induced bubbles between graphene and hBN. In addition, the inherent wrinkles of graphene during the growth process will survive in the dry-transfer process, thus contributing to a part of low ratio of $I_{2D/G}$.

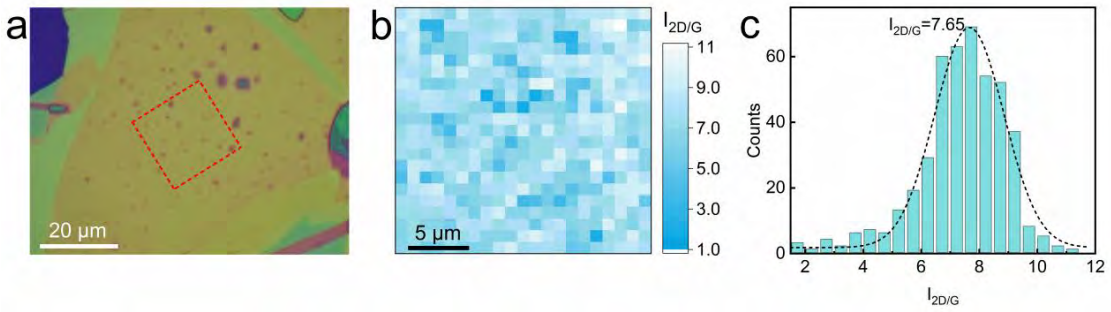

Figure S3. Statistical analysis of $I_{2D/G}$ ratio of as-transferred graphene encapsulated by hBN. a) The optical image of hBN/Graphene/hBN heterojunction. b) The mapping of $I_{2D/G}$ corresponding to the red dashed box area in (a). c) Histogram of the $I_{2D/G}$ of the heterojunction.

Supporting Section 4: Extraction of the charge-carrier mobility by Drude model

As the most important parameter for electrical properties in graphene, the values of the density-dependent mobilities in the main text are extracted by Drude model. The concrete value of the mobility μ_{D} is calculated from the equation $\mu_{\mathrm{D}} = \sigma/ne$, where σ is the conductance of the Hall device and *e* is the elementary charge. As a function of the back-gate voltage V_{bg}, the carrier density *n* is obtained from the linear fitting through the Hall measurement as shown in Figure S4a, in which the linear relationship is consistent with the formula $n = C_{\mathrm{g}}\left(V_{\mathrm{bg}} - V_{\mathrm{Dirac}}\right)/e$.[4] Here C_{g} is the gate capacitance of Hall devices, V_{Dirac} is the Dirac point of the graphene and *e* is the elementary charge.

It has been proved that a self-consistent Boltzmann model fits better with the transport curve of four-terminal conductance σ, especially at high carrier density.[5] In this model, the nonlinear relationship is given by the following formula:

$$\sigma^{-1} = (ne\mu + \sigma_0)^{-1} + \rho_s \qquad \text{(S1)}$$

Here μ is the mobility, ρ_s is the residual resistivity related to short-range scattering effect and σ_0 is the conductivity near the charge neutral point. The above model often lead to a higher carrier mobility value at low carrier density.[2] Alternatively, the carrier mobilities μ of graphene can also be estimated conservatively by dealing with the $\sigma - n$ curve (nattier blue) near the Dirac point according to linear fitting (red dotted line) as shown in Figure S4, where the mobilities of electrons and holes are calculated as 8.3×10^4 $\mathrm{cm^2V^{-1}s^{-1}}$ and 11.5×10^4 $\mathrm{cm^2V^{-1}s^{-1}}$ respectively.[6] From this method, the maximum mobility is higher than the value as demonstrated in the main text.

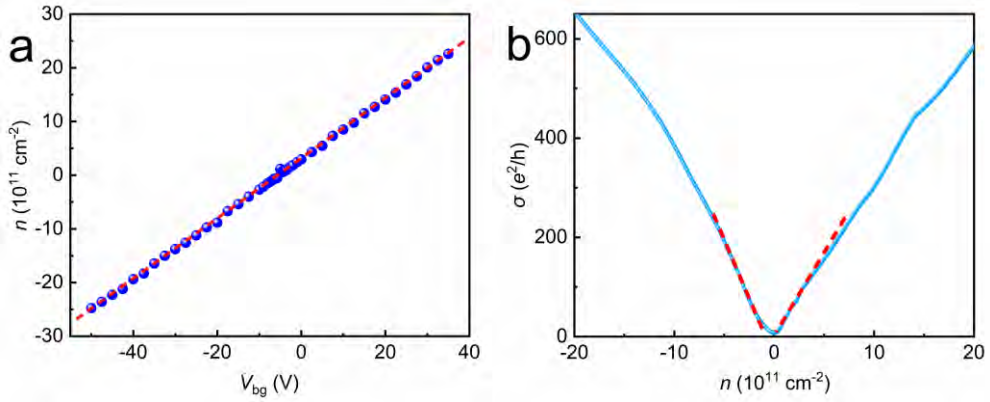

Figure S4. Linear fitting of conductance curve. a) Linear fitting of the carrier density n at different back-gate voltage V_{bg} obtained from Hall measurement. b) Linear fitting to the conductance as function of the charge-carrier density n near the Dirac point according to the Drude model. The mobilities of electrons and holes are extracted from the formula: $\mu = \frac{1}{e}\frac{\mathrm{d}\sigma}{\mathrm{d}n}$, in which the accurate values for electrons and holes are 8.3 × 10^4 $cm^2V^{-1}s^{-1}$ and 11.5 × 10^4 $cm^2V^{-1}s^{-1}$ respectively.

The relationship of four-terminal resistance R and back-gate voltage V_{bg} of other four Hall devices are plotted in Figure S5 and the corresponding carrier density fluctuations n^* are extracted in the inset of each diagram.[7] Following the same linear fitting procedure as Figure S4b, the specific electrical parameters (i.e. the mobilities μ of electrons and holes, the carrier density fluctuations n^*) of all five devices at 2.3 K are extracted and summarized in Figure S6.

In summary, all devices exhibit small carrier density fluctuations n^* less than 10^{11} cm^{-2} and the drastically reduced potential fluctuations result in high mobilities ranging from 4.5 × 10^4 $cm^2V^{-1}s^{-1}$ to 11.5 × 10^4 $cm^2V^{-1}s^{-1}$. The extremely high mobilities in sandwiched graphene grown on Ge(110) provide an opportunity for the observation of fractional quantum Hall effect (FQHE) as demonstrated in Figure S7.

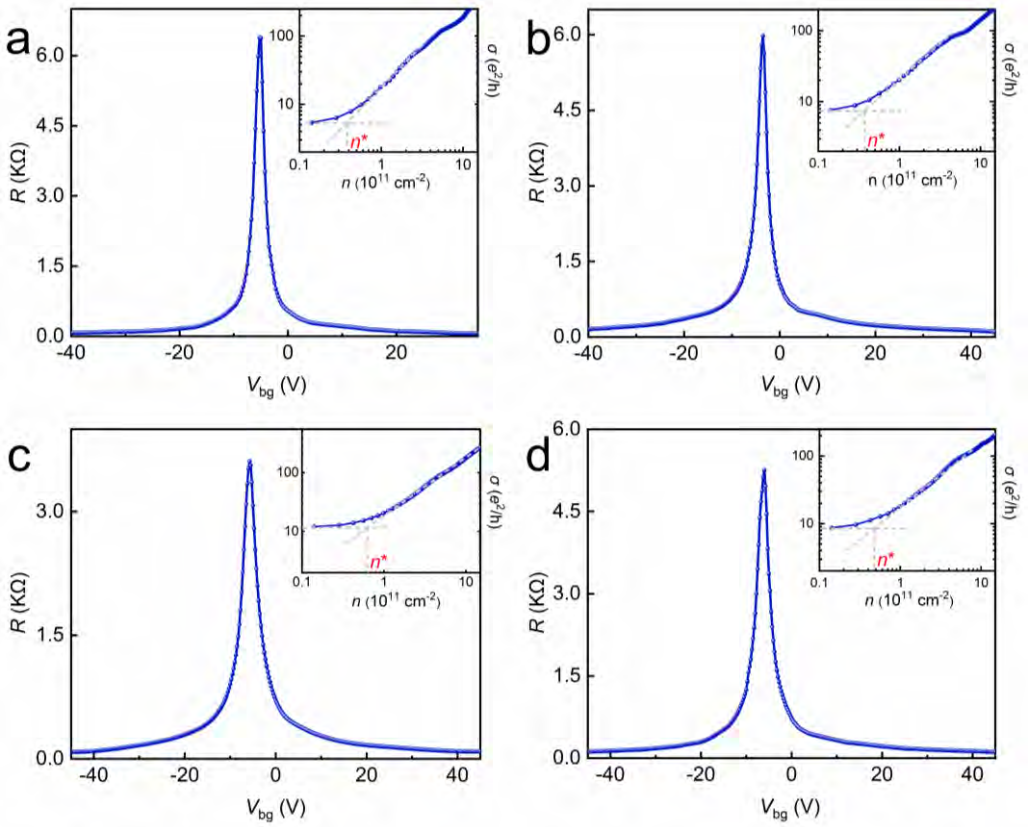

Figure S5. Four-terminal resistance R as a function of back-gate voltage V_{bg} at 2.3 K for other 4 devices（a-d）. The inset shows the disorder induced charge carrier density fluctuations n^* obtained by the corresponding $R - V_{\mathrm{bg}}$ curve. Here, σ is the four-terminal conductance of the device.

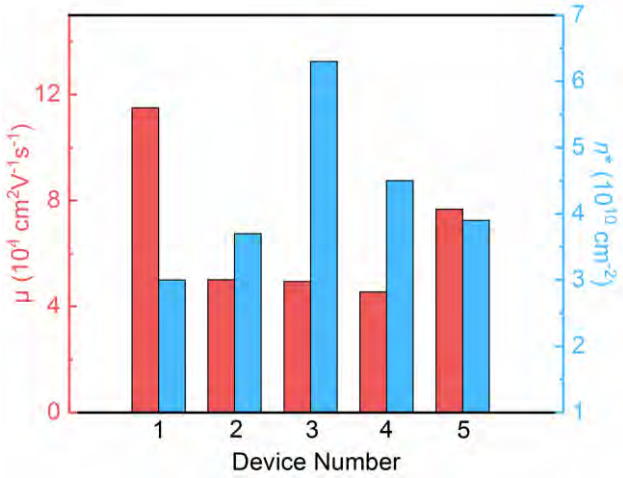

Figure S6. The maximum mobility μ (red) and carrier density fluctuations n^* (light blue) of 5 different devices at 2.3 K. The mobility are extracted from the linear fitting near the Dirac point as illustrated in Figure S5b and the carrier density fluctuations n^*

(blue) is extracted as shown in the inset of the Figure S5.

Supporting Section 5: Observation of fractional quantum hall effect (FQHE)

At low carrier density, the electrons in half-integer quantum Hall regime are confined in discrete Landau levels as demonstrated in Figure 4 in the main text. In this case, the carriers in graphene can be treated as massless Dirac fermions and their Coulomb interactions are negligible. When a higher back-gate voltage V_{bg} (45 V) is applied, the SdH oscillations of magnetoresistance R_{xx} is gradually distorted under high magnetic field and the $R_{xx} - B$ curve in Figurer S7 cannot be well described by formula (3) shown in the main text. In particular, more weak Hall plateaux and corresponding oscillations of magnetoresistance occur between filling factors $\nu = 14$ and $\nu = 18$ as shown in the inset. The unexpected filling factors, $\nu =$ 76/5, 111/7 and 17 (denoted as colored dotted line) arise from the splitting of Landau levels, in which the composite quasiparticles (or composite fermions) are bound with magnetic flux quanta and electrons, and thus manifest fractional electronic charge.[8] The emergence of the fractional quantum Hall states in hBN-encapsulated graphene can be regarded as an signal of extremely high mobility. Limited by temperature (2.3 K) and magnetic field (0 - 9 T), more details of fractional quantum Hall effect in sandwiched graphene need to be explored under lower temperature and stronger magnetic field.

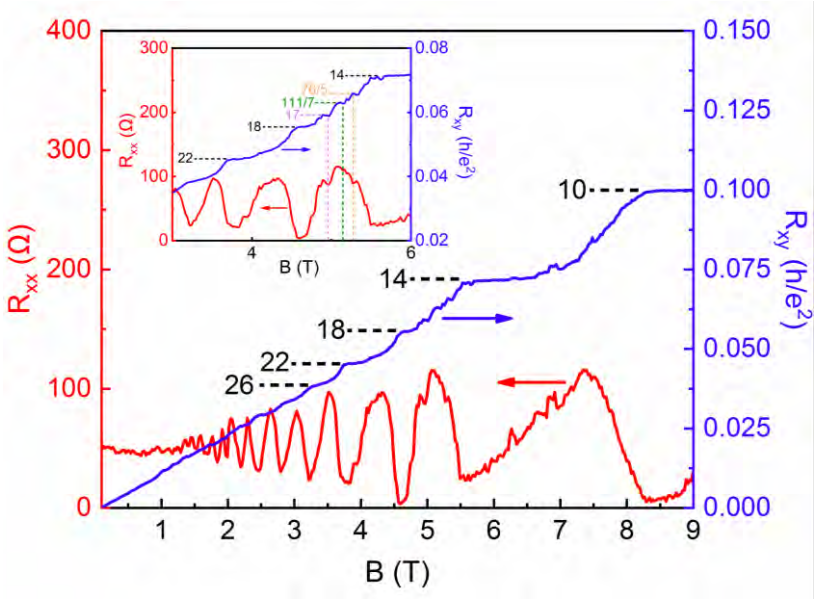

Figure S7. Fractional quantum hall effect of sandwiched graphene. Inset: the anomalous quantum hall plateaux occur between filling factor $\nu = 14$ and $\nu = 18$.

Supporting References

[1] L. Lin, J. C. Zhang, H. S. Su, J. Y. Li, L. Z. Sun, Z. H. Wang, F. Xu, C. Liu, S. Lopatin, Y. H. Zhu, K. C. Jia, S. L. Chen, D. R. Rui, J. Y. Sun, R. W. Xue, P. Gao, N. Kang, Y. Han, H. Q. Xu, Y. Cao, K. S. Novoselov, Z. Q. Tian, B. Ren, H. L. Peng , Z. F. Liu, *Nat. Commun.* **2019**, *10*, 7.

[2] L. Banszerus, M. Schmitz, S. Engels, J. Dauber, M. Oellers, F. Haupt, K. Watanabe, T. Taniguchi, B. Beschoten , C. Stampfer, *Science Advances* **2015**, *1*, 6.

[3] C. Casiraghi, S. Pisana, K. S. Novoselov, A. K. Geim , A. C. Ferrari, *Appl. Phys. Lett.* **2007**, *91*, 3.

[4] Y. B. Zhang, Y. W. Tan, H. L. Stormer , P. Kim, *Nature.* **2005**, *438*, 201.

[5] N. Petrone, C. R. Dean, I. Meric, A. M. van der Zande, P. Y. Huang, L. Wang, D. Muller, K. L. Shepard , J. Hone, *Nano Lett.* **2012**, *12*, 2751.

[6] D. De Fazio, D. G. Purdie, A. K. Ott, P. Braeuninger-Weimer, T. Khodkov, S. Goossens, T. Taniguchi, K. Watanabe, P. Livreri, F. H. L. Koppens, S. Hofmann, I. Goykhman, A. C. Ferrari , A. Lombardo, *ACS Nano.* **2019**, *13*, 8926.

[7] N. J. G. Couto, D. Costanzo, S. Engels, D. K. Ki, K. Watanabe, T. Taniguchi, C. Stampfer, F. Guinea , A. F. Morpurgo, *Physical Review X.* **2014**, *4*, 13.

[8] K. I. Bolotin, F. Ghahari, M. D. Shulman, H. L. Stormer , P. Kim, *Nature.* **2009**, *462*, 196.